JAAS

A Transmission-Type Triple Grating Spectrograph for Improved Laser Scattering Diagnostics of Low-Density Plasmas used in Chemical Analysis

Journal:	*Journal of Analytical Atomic Spectrometry*
Manuscript ID	JA-ART-04-2020-000193.R1
Article Type:	Paper
Date Submitted by the Author:	01-Jun-2020
Complete List of Authors:	Finch, Kevin; Texas Tech University, Department of Chemistry and Biochemistry Hernandez, Aldo; Texas Tech University, Department of Chemistry and Biochemistry She, Yue; Texas Tech University, Department of Chemistry and Biochemistry Shi, Songyue; Texas Tech University, Department of Chemistry and Biochemistry Gamez, Gerardo; Texas Tech University, Department of Chemistry and Biochemistry

SCHOLARONE™
Manuscripts

1
2
3
4
5
6
7
8
9
10
11
12
13
14
15
16
17
18
19
20
21
22
23
24
25
26
27
28
29
30
31
32
33
34
35
36
37
38
39
40
41
42
43
44
45
46
47
48
49
50
51
52
53
54
55
56
57
58
59
60

Table of Contents Figure
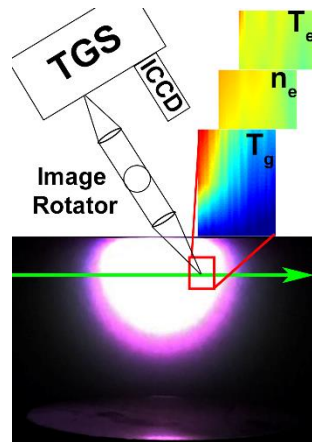
An improved transmission-type triple grating spectrograph permits 2D mapping of plasma species via laser scattering closer to surfaces, at faster measurement times, and the lowest electron density detection limit reported.

1
2
3 Primary Manuscript
4
5
6
7
8
9
10
11
12
13 **A Transmission-Type Triple Grating Spectrograph for Improved Laser Scattering**
14 **Diagnostics of Low-Density Plasmas used in Chemical Analysis**
15
16
17
18
19 Kevin Finch, Aldo Hernandez, Yue She, Songyue Shi, Gerardo Gamez*
20
21
22
23
24
25 Texas Tech University, Department of Chemistry and Biochemistry, Lubbock, TX, 79409-41061,USA
26
27 *Corresponding author. Phone: (806) 834-846 Email: gerardo.gamez@ttu.edu
28
29
30
31
32
33
34
35
36
37
38
39
40
41
42
43
44
45
46
47
48
49
50
51
52
53
54
55
56
57
58
59
60

A Transmission-Type Triple Grating Spectrograph for Improved Laser Scattering Diagnostics of Low-Density Plasmas used in Chemical Analysis

Kevin Finch, Aldo Hernandez, Yue She, Songyue Shi, Gerardo Gamez*

Abstract

A wide variety of plasma geometries and modalities have been utilized for chemical analysis to date, however, there is much left to be understood in terms of the underlying mechanisms. Plasma diagnostics have been used for many years to elucidate these mechanisms, with one of the most powerful techniques being laser scattering approaches. Laser scattering provides information about the energetic species distributions, in terms of kinetic energy and densities, which can provide invaluable insights into the fundamental processes of chemical analysis plasmas with minimal perturbation. Thomson scattering (TS) from free electrons is the most difficult to implement due to the extremely stringent instrumental requirements for discerning the signal from competing scatterers in low-density plasmas, such as those seen in analytical chemistry applications. Nonetheless, relatively few instruments have been developed to satisfy these stringent requirements. In this paper, the design and characterization of a transmission-type triple grating spectrograph (TGS), with high numerical aperture (0.25)/contrast ($\leq 10^{-6}$ at 532 ± 0.5 nm)/stray light rejection (~1.8×10^{-8} at 532 ± 22-32 nm) required for TS, will be presented. In addition, proof-of-principle measurements on glow discharges operated under typical optical emission spectroscopy (OES) conditions demonstrate the high light throughput and low limits-of-detection (~10^9 cm^{-3} at ~1 eV T_e) afforded by the new instrument.

1. Introduction

Plasmas are widely accepted as one of the most versatile sources of excitation and ionization for performing chemical analyses on a plethora of sample types [1-17]. Due to the popular nature of these sources, there are a variety of geometries and modalities being rapidly developed to improve their analytical performances through trial-and-error approaches. However, the underlying plasma species' energy/density distributions are not well characterized for many of the novel source geometries and modes of operation. Moreover, some of the plasmas that have been commonly studied, such as inductively couple plasmas (ICPs), have fundamental aspects that would benefit from further fundamental studies [18-24]. Therefore, there is a need to perform plasma diagnostics to gain insights into the spatiotemporal behavior of species of interests and their underlying mechanisms. Furthermore, these insights will allow the improvement of the plasma

analytical performance through rational design strategies, as opposed to trial-and-error approaches that may only lead to partial optimization.

Although there are many diagnostic procedures used to perform fundamental plasma studies [25-30], laser scattering techniques [31-35] give direct access to several important plasma parameters and have inherent advantages in comparison with Langmuir probes or optical emission spectroscopy (OES). Scattering techniques offer ease of data analysis, direct probing of plasma species, no assumption of local thermodynamic equilibrium (LTE), inherent radial (when plasma radius > laser beam width) and temporal resolution, and little-to-no perturbation of the plasma (with simple control of the laser fluence) [26, 36-38]. On the other hand, disadvantages may include complex and expensive experimental requirements for accurate plasma diagnostic measurements. Therefore, laser scattering is the method of choice when the appropriate instrumentation is available [22, 37, 39-42].

Thomson scattering is the elastic scattering of radiation by unbound charges interacting with an incident electromagnetic wave [43]. Free electrons are the primary species probed by this technique due to their inherently low mass and ability to respond to the fast field changes of the incoming radiation. Due to the motion of electrons within plasmas, in relation to the laser beam and detector, the frequency of the scattered radiation is noticeably Doppler shifted [43]. When studying relatively low-temperature and low-density plasmas, the scattering is incoherent [44]. In this case, the Thomson scattered spectrum is representative of the electron energy distribution function (EEDF) as described by Huang et al. [44], while allowing for simultaneous measurements of electron temperature (T_e), from the shape of the spectrum, and electron density (n_e), proportional to the area without the compounding of error from one calculation to the next. [22, 43, 44]. If the EEDF follows a Maxwellian distribution, then the width of the Doppler shifted Thomson signal will directly relate to the T_e [45].

Rayleigh Scattering is the elastic scattering of radiation by electron clouds bound to heavy particles capable of a dipole moment change in the plasma i.e. atoms, ions, and molecules [46]. The majority of these heavy particles are gas atoms due to them being the highest concentration of scatterers present [43]. The Rayleigh signal is found centered at the same wavelength as the incident light and its intensity is directly proportional to the number density of gas atoms (n_g) while being inversely proportional to the gas-kinetic temperature (T_g), via the ideal gas law [45, 47]. Rather elegantly, Rayleigh scattering also allows for the absolute calibration of the n_e obtained via Thomson scattering, through the ratio of the corresponding scattered intensities at a known n_g [48].

Raman scattering is the inelastic scattering of radiation by molecules capable of a polarizability change after interacting with an incident electromagnetic wave [46]. The

scattered radiation has a wavelength shift, in relation to the incident light, based on the associated transition in the rotational or vibrational state of the molecule. The rotational temperature (T_{rot}), vibrational temperature (T_{vib}), and molecular densities can be derived by fitting simulated Raman spectra to the experimental data [46]. When molecular species are present in the plasma of interest (i.e. atmospheric jets, nitrogen torches, etc.), the Thomson signal will be spectrally overlapped by rotational Raman scattering, but there are well-documented deconvolution schemes, based on polarization control [49] or simulated spectra [46], that have been implemented.

Thomson scattered radiation is among the most difficult to accurately measure due to the very small electron cross-sectional area, and relatively small Doppler shifts (corresponding to relatively low T_e), which place the signal extremely close to the orders-of-magnitude higher Rayleigh signal located at the laser's central wavelength. The Rayleigh scattered differential cross-section has values that can be $> 10^7$ times greater than the Thomson differential cross-section [16, 32, 50]. Furthermore, the concentration of the Rayleigh scatterers is orders-of-magnitude higher than the concentration of free electrons, which places a large burden on achieving high spectral contrast under these conditions to apply suitable detector gain levels without saturation. The relatively weak Thomson signal is attenuated even further in low-density plasmas, arising from the low degree of ionization and in turn relatively low n_e populations ($n_e \leq 10^{14}$ cm^{-3}). Additionally, stray light from high intensity lasers can unacceptably lower the signal-to-noise ratio (S/N), especially at observation regions near highly reflective surfaces/walls and is thus crucial to minimize. On the other hand, the stringent experimental requirements make complementary laser scattering studies (Rayleigh and Raman) easy to implement with little-to-no changes of the existing instrumentation [46, 51].

Thus, highly efficient wavelength selection devices (contrast $\leq 10^{-6}$ at ± 0.5 nm shifts and f-number $\leq F/6$) must be utilized to overcome the aforementioned difficulties in acquiring the Thomson scattering signal from low-density plasmas, many of which are implemented for chemical analysis. Gamez et al. designed an instrument to allow Thomson scattering on a low-density planar-cathode direct current (DC) glow discharge (GD), which provided many insights into the underlying mechanisms [37]. The instrument featured a double monochromator that was used first as a single spatial position monitoring system via a photomultiplier tube to study a continuous DC GD [41]. It was improved in 2005 through the addition of an iCCD for multiple spatial position monitoring of ms-pulsed DC GD [42]. However, the instrument was set to allow only a 0.3 nm wavelength band to pass at any given time, such that the wavelength was required to be scanned for performing spectral measurements. The authors report very long acquisition time (~6 hours) for only one-half of the symmetric Thomson scattering spectrum. Furthermore, stray light limitations prevented measurements closer than 4 mm

to the cathode. On the other hand, triple grating spectrographs (TGSs) can yield better stray-light rejection, along with better contrast, closer to the laser wavelength, albeit with a more complicated setup. Also, a TGS coupled with an array detector allows obtaining the whole Thomson scattering spectrum at multiple spatial positions, thus lowering the required measurement time. There are only a few commercially available TGS that are in production today. However, commercial TGSs have high costs (~$100,000) and are on the edge of the wavelength selection device requirements to perform TS on low-density plasmas (e.g. f-numbers that range from F/4.8 [52] to F/7.5 [53]). A reflection-type TGS was previously constructed in 2002 by M. J. van de Sande and J. J. A. M. van der Mullen, to study low-density plasmas via Thomson scattering [36] and the design is described in further detail within M.J. Van de Sande's Ph.D. thesis [32]. Thomson measurements were able to be taken < 0.5 nm away from the central wavelength due to the high contrast and stray-light rejection. There has been successful implementation of this TGS on multiple plasmas including low and high pressure gas discharge lamps [36, 54-56] and a plasma jet at atmospheric pressure [46]. Nonetheless, this particular TGS has a low throughput with only 10% of light passing to the detector and a relatively low collection efficiency of F/6.3 [36]. In 2017, during the initial stages of the instrument construction discussed herein, Chalyavi et al. published an article reporting on the development of a transmission-type TGS at Agilent Laboratories [49]. This TGS provides a higher light collection efficiency (F/2), transmission (> 70% at 532 nm ± 2.5 nm), and was initially tested on an Ar ICP, [49] which has a relatively high n_e of ~10^{15} cm^{-3}. The system was then used to probe a microwave induced plasma sustained in N_2 [49] (used in Agilent's 4200 MP-AES instrument that was commercialized in 2011 [57]) and reported a single value for the n_e and T_e that, together with Boltzmann plots and collisional-radiative modeling, was used to assess LTE but comparisons with low-density plasma studies are difficult. Furthermore, the large size of the gratings chosen for this TGS produce a significant smile (curvature of the slit image) aberration due to the larger change in dispersion angle at further field positions from the central optical axis [58].

Most recently, in 2018, Vincent et al. developed a novel compact diagnostic instrument that the authors named *Thomson scattering experiments for low temperature ion sources-incoherent Thomson scattering* (THETIS-ITS) [59]. This instrument uses a single volume Bragg grating (VBG) notch filter scheme (Transmission 10^{-3} to 10^{-4} at 532 ± 0.2 nm, > 96% at 532 ± 0.3 nm) prior to a commercial single spectrograph and was successfully used to obtain TS spectra on an atmospheric pressure plasma jet [59]. Although high throughput is desirable, this high transmission and relatively low contrast can be detrimental at close wavelength shifts in terms of stray light and Rayleigh signal overlap, particularly for low n_e measurements performed very close to reflective surfaces. Furthermore, the VBG notch filter bandwidth cannot be changed to obtain a higher contrast when necessary. Finally, the physical size of the VBG is a limitation for

achieving high light collection efficiency when collection optics cannot be placed in close proximity to the plasma.

In this paper, based on the advantages and limitations described above, we present the design of a newly constructed TGS for improved laser scattering diagnostics of low-density plasmas. The corresponding key figures-of-merit of spatial/spectral resolution and contrast are characterized. In addition, proof-of-principle measurements are reported on continuous DC, and ms-pulsed radiofrequency (RF) GDs, which are a good model system due to the inherently low degree of ionization, relevant information close to walls/surfaces, and availability of some literature for comparison/validation purposes[8]. The demonstrated improved features of high transmission/contrast/stray light rejection result in faster measurement time and the ability to get closer to walls/surfaces. Thus, this instrumentation will allow more systematic and in-depth characterization of the fundamental parameters in low-density plasmas used in chemical analysis, leading to an improved understanding of their underlying mechanisms.

2. TGS design
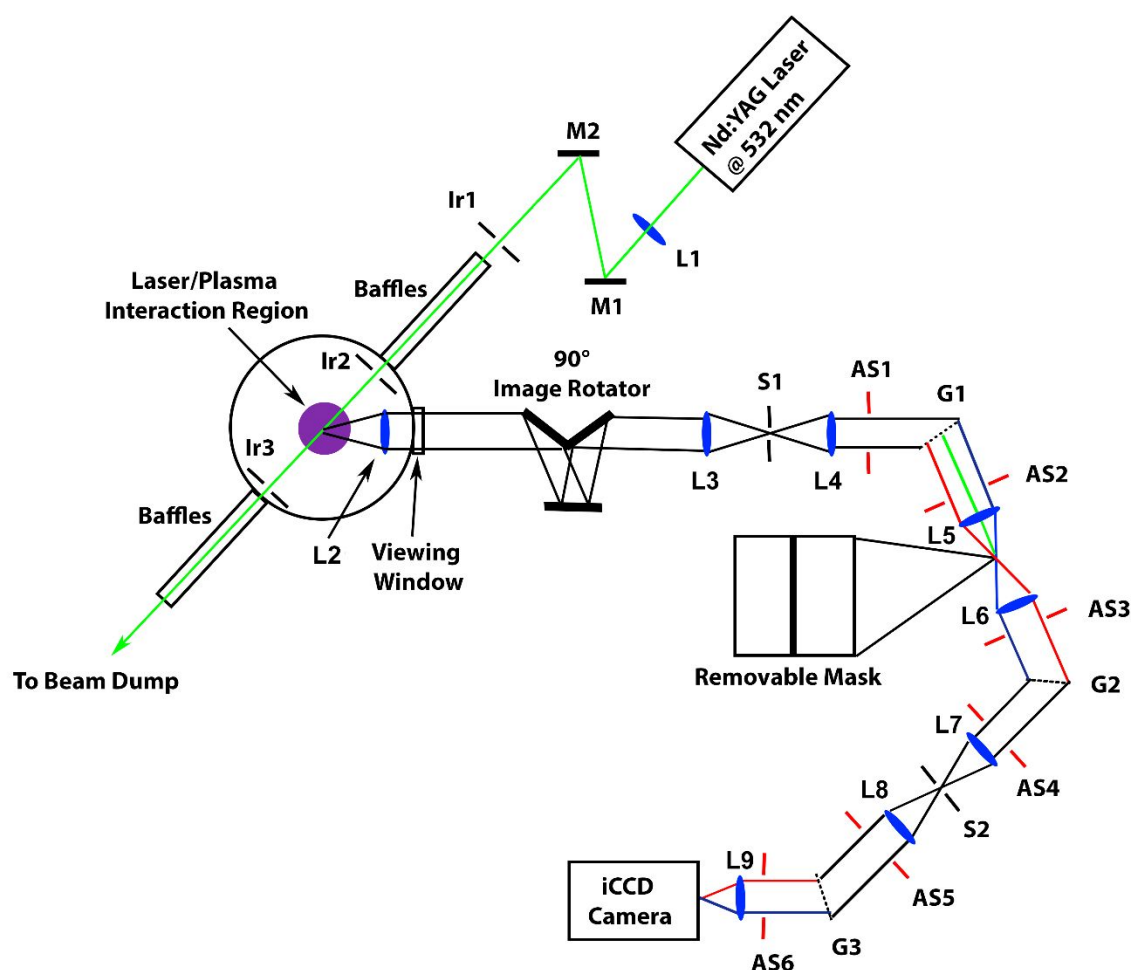
Figure 1. Top view schematic of the TGS instrument with collection optics and experimental setup for studying a planar-cathode GD. (see Table 1 for specifications). A narrowband notch filter is created by the first two TGS stages in subtractive mode where a removable mask is placed in between to physically block the transmission around 532 nm.

Table 1. Specifications of components in the experimental setup. (see Fig. 1)

Optical Component	Description
Laser	Nd:YAG @ 532 nm, 20 Hz (Continuum® Powerlite 8020)
Laser Focusing Lens (L1)	50 mm Ø, 1029.8 mm FL Biconvex (Melles Griot)
90° Image Rotator	K-mirror design: 76.2 mm Ø plane mirrors, (BB3-E02, Thorlabs)
Collection Lenses (L2-L3)	50 mm Ø F/2 planoconvex singlets (Melles Griot)

TGS Lenses (L4-L9)	50 mm Ø F/2 aspheric, AR coating <0.5% reflection @ 532 nm (AL50100-A, Thorlabs)
Volume Phase Holographic Transmission Gratings	50.8 mm Ø, 1800 lines/mm, 28.6° AOI @ 532 nm, AR coating <0.5% reflection @ 532 nm (Wasatch Photonics)
Slits	13 mm height x 52 μm width (National Aperture)
Removable Mask	13 mm height x 0.33 mm width (National Aperture)
Aperture Stops (AS1-AS6)	39.5 mm width x 45 mm height elliptical (TTU Machine Shop)
iCCD Camera	13.3 mm x 13.3 mm detector size, 13 μm pixel width/height (iStar 334T, Andor)

The experimental setup for this custom designed transmission-type TGS and its application to a planar-cathode GD is shown in Fig. 1. The GD chamber shown here was described by Gamez et al in 2003 [37]. A frequency-doubled ($\lambda_i = $ 532 nm) Q-switched Nd:YAG laser produces about 40 mJ, ~6 ns pulses at a repetition rate of 20 Hz. The Gaussian beam is steered into the GD chamber using two dichroic mirrors, laser coated at 532 nm. The beam is focused into the center of the plasma by L1, giving a beam diameter of ~0.5 mm, resulting in a laser fluence of ~20×10^4 J/m² that prevents plasma heating by the laser through inverse bremsstrahlung processes. An iris (Ir1) is used to "clean" up the beam edges prior to passing through the entrance Brewster's window [37]. The GD chamber arms feature baffles and two irises (Ir2 and Ir3) to minimize the stray light generated at the entrance/exit windows from reaching the laser/plasma interaction region [37]. A pair of lenses (L2 and L3) are used to collimate and subsequently focus the image onto the entrance slit (S1) of the TGS. The high numerical aperture (0.25), and thus high light collection efficiency, is matched to the TGS. The geometry of a 135° scattering collection angle was chosen to minimize the Rayleigh signal and to ensure the scattering was incoherent ($a \ll 1$). There is an additional 50.8 mm diameter window that is placed in between the active plasma region and the collimating lens (L2) to prevent sputtered material from depositing on the lens. A 90° image rotator (K-mirror design [60]) is incorporated between L2 and L3 to align the horizontal laser beam with the TGS vertical entrance slit (S1) for radially resolved information to be collected simultaneously. The slit width was chosen taking into account geometric extent and spectral resolution requirements for TS. The aspheric lens (L4) after the entrance slit collimates the light which goes through an elliptical aperture stop (AS1) that matches the projected cross-section dimensions on the tilted grating. Similar elliptical aperture stops (AS1-AS6) are placed along the TGS to lower stray light transmission. The first transmission-type volume phase holographic grating (G1) disperses the light prior to being refocused onto a physical, removable mask by L5 that maximizes the attenuation at 532 nm. These transmission gratings were specifically utilized to ensure compact instrument design with the optimal efficiency at the same polarization state as the Thomson scattering.

1
2
3
4
5
6
7
8
9
10
11
12
13
14
15
16
17
18
19
20
21
22
23
24
25
26
27
28
29
30
31
32
33
34
35
36
37
38
39
40
41
42
43
44
45
46
47
48
49
50
51
52
53
54
55
56
57
58
59
60

Furthermore, the grating size, smaller compared to the TGS described in [49], was chosen to minimize smile distortions while maintaining a high optical throughput. The mask width (0.33 mm) is chosen to obtain at least 10^{-6} contrast at ± 0.5 nm from the central wavelength. L6 collimates the light into a second identical grating (G2) that cross-disperses the light, undoing the dispersion created by G1, prior to being refocused by L7 onto the intermediate slit (S2). The third stage acts as a single spectrograph, dispersing the light a final time via G3 and focusing the image (with the 532 nm band minimized) onto the iCCD camera by L9 for subsequent detection. Each of the three stages has been separated by physical barriers that minimize stray light outside of the optical axis. A light-tight box was constructed to encompass L3 to the iCCD camera that features self-adhesive Hi-Tack flocked light trap (ProtoStar) inside lining that has a spectral reflectivity < 1 % @ 532 nm. The high efficiency antireflection (AR) coated optics and large numerical aperture (0.25, F/2) were chosen to maximize light throughput with a nominal transmission of ~70% @ 532 nm for the TGS.

3. Experimental methods

The TGS was characterized in terms of the imaging qualities, spectrograph performance, and notch filter efficiency. Specifically, the flatfield response, spatial and spectral resolutions, and notch filter contrast were measured. The flatfield images were taken by placing a home-built diffuser, composed of multiple layers of translucent cellophane tape, adjacent to S1 and illuminating it with an LED spotlight source (Advanced Illumination SL2420). The image to determine spectral resolution was obtained in a similar fashion but replacing the LED lamp with a Ne pen-ray lamp (Analytik Jena 90-0015-01). Spatial resolution images were also collected this way but with the addition of a "lined mask" (parallel lines ~1.5 mm thick separated by ~2 mm oriented across the slit) to the diffuser at S1 and LED illumination. The notch filter contrast was measured by imaging the Rayleigh scattering produced in the GD chamber, filled with Ar at atmospheric pressure, using the Nd:YAG laser beam. First, an image was taken without the physical mask in place to measure a nominal intensity value at 532 nm. Low iCCD gain and addition of an OD4 neutral density filter (Thorlabs NDUV40B) at S1 was necessary to increase the dynamic range of the measurement to ≥ 6 orders-of-magnitude. Then, the physical mask was added to minimize the transmission of the 532 nm band and the stray-light around the mask was measured after removing the ND filter and applying a higher iCCD gain.

The spatial resolution and flatfield at the object of interest (GD chamber) (see Fig. 1) were also measured. The flatfield image was obtained by placing a 600-grit ground glass diffuser (Thorlabs DG100X100-600) along the laser axis, focal point of L2, in the center of the GD chamber for the LED ring lamp's light to be spatially homogenized. A 1951 USAF target mounted on an xy translation stage was then placed adjacent to the

1
2
3
4
5
6
7
8
9
10
11
12
13
14
15
16
17
18
19
20
21
22
23
24
25
26
27
28
29
30
31
32
33
34
35
36
37
38
39
40
41
42
43
44
45
46
47
48
49
50
51
52
53
54
55
56
57
58
59
60

diffuser and several images were obtained at different positions to measure the spatial resolution at the center of the plasma/laser interaction region. A baseline correction algorithm written in Matlab® with the function "msbackadj" from the bioinformatics toolbox, was used to remove the background contribution in the target images. The flatfield and spatial resolution images both had a smile of the mask that was straightened with an algorithm written in Matlab® using the function "imwarp". The resulting images were then subsequently filtered using a median filter with a neighborhood of 3 pixels, followed by a 2-pixel moving average, both applied only in the spatial dimension. The warping was performed so a final normalization scheme to the average pixel response per column described by Hieftje et al. in 1989 [61] could be implemented to correct all subsequent images for system aberrations and intensity differences.

During the laser scattering studies the laser pulses (~6 ns, 20 Hz) and iCCD gate (20 ns gate width) were synchronized. The laser power was measured at the beginning and end of each measurement, to account for power drift, using a fast photodiode (Newport 818-BB-20) calibrated with a laser power meter equipped with a high-energy attenuator (Gentec QE25LP-S-MB-QED). Rayleigh and Thomson measurements were taken in Ar (99.999%) and Raman measurements were taken in N_2 (99.999%). A combination pressure gauge (MKS series 910), mass flow controller (Cole-Parmer 32907-69), and a roughing pump (Leybold TRIVAC D-25-B) equipped with an adjustable valve were used to maintain the desired pressure in Torr.

Rayleigh scattering studies were performed by operating the GD in DC power mode. A DC power supply (Spellman PTV Series) was connected to the cathode assembly with an 11 mm diameter stainless steel (SS) cathode, separated by a 35 mm interelectrode distance from the 50 mm diameter SS grounded anode. The cathode was also cooled to 20° C with a recirculating chiller (Thermo Neslab Merlin M25). Images (150 replicates) were taken under the following conditions: An integration time of 2 s (40 laser shots), 3x binning spectrally, 8x binning spatially, and 3750 gain level. Background images were taken under the same conditions at the end of each Rayleigh study. 2D maps were created by taking measurements at three different heights from the cathode (3, 5, 7 mm axially) and at the edge of the negative glow region (4.8 - 8 mm radially). The data was then 2D interpolated in Matlab® with the function "interp2" using a step size of 0.1 mm.

Thomson scattering studies were performed by operating the GD in pulsed RF power mode. The RF power supply (Comet Cito-1350-WC7B-N37A-FF) and impedance matching network (Comet AGS-1350W-MB) were connected to the cathode assembly with an 11 mm diameter Ni cathode, separated by a 25 mm interelectrode distance to a 50 mm diameter SS grounded anode. The cathode was cooled to 20° C. The RF pulses (2 ms pulse duration at a 20% duty cycle) were synchronized with both the laser and the iCCD

gate. The negative DC self-bias (V_{dc}) was measured with an oscilloscope (Agilent InfiniiVision DSOX3034A) through a high voltage probe (Tektronix P6015A, 1000:1) at the base of the cathode assembly. The V_{dc} was adjusted to either 250 or 500 V (see SF1) before probing the plasma 4 μs before the end of the 2 ms RF pulse (see SF2). Images (plasma and laser on) were taken under the following conditions: An integration time of 10 min (12000 laser shots), 3x binning spectrally, 8x binning spatially, and 4095 gain level for the 2D maps. The gain was lowered to 3500 for obtaining the image centered in the plasma at a radial position of 0, to calculate the best n_e limit-of-detection (LOD) achievable. Background images (plasma on and laser off), for subsequent subtraction, were taken directly after each Thomson measurement to account for plasma fluctuations more accurately. A flatfield correction was then applied to each Thomson image after filtering with a 3-pixel median filter, followed by a 2-pixel moving average, both applied only in the spatial dimension. Five replicates were then averaged together for statistical purposes. 2D maps were created by taking measurements at two different heights from the cathode (2.5, 5 mm axially) and at the edge of the negative glow region (4.8 - 8 mm radially). The data was then 2D interpolated in Matlab® with the function "interp2" with a step size of 0.1 mm. The T_e was extracted from the Thomson scattering spectra by creating a "linearized" plot of natural log of the scattering signal vs the wavelength shift squared, where the slope of the linear regression is inversely related to the T_e. Five replicates were used for subsequent T_e error calculations based on the standard deviation of the slope for the linear regression, created by using all the replicate data points simultaneously. The n_e values were extracted by fitting a single Gaussian distribution to the Thomson scattering spectra, at each radial position, using an algorithm written in Matlab® with the function "fit". The area under this fitted curve is directly proportional to the n_e and can be absolutely calibrated via Rayleigh scattering. The error in the n_e was evaluated by using the χ^2 value obtained from the fitted Gaussian curve for all replicates simultaneously based on the relationship to the standard deviation [62]. For this study, a unique scheme was employed for absolute calibration using the relationship between the Raman and the Rayleigh signals. It is possible to remove the TGS physical mask that blocks the laser wavelength to measure Rayleigh scattering for day-to-day calibration. Here, however, the Raman scattering was used for day-to-day calibration, by standardizing it to the Rayleigh signal, which is best for time and reproducibility purposes because it does not require daily removal of the mask. Initially, the chamber is purged 3x and filled with N_2 to atmospheric pressure at room temperature for obtaining the Raman signal. Then, at each radial position, the intensity values at 3 specific wavelength shifts (533, 534, 535 nm) in the Raman spectra (with mask) were used to draw a linear relationship to the Rayleigh peak intensity at 532 nm (without mask). Then, each day a Raman scattering image, taken at the same camera conditions that will be used for Thomson measurements, was used to related to the Rayleigh peak intensity through

the linear correlation. Direct Rayleigh scattering calibration vs the unique Raman scheme found < 1% deviation, which verifies the reliability of this technique.

Raman scattering studies were performed with the plasma off and the GD chamber purged and filled to atmospheric pressure with ultra-high purity N_2 for the inclusion of molecular species. Images were taken under the following conditions: An integration time of 5 min (6000 laser shots), 1x binning spatially, 1x binning spectrally, and 3500 gain. Background images were taken under the same conditions at the end of each Raman image for subsequent subtraction. A 3-pixel median filter followed by a 2-pixel moving average, both in the spatial dimension, were applied before the flatfield correction. The data was then 2D interpolated in Matlab® with the function "interp2" with a step size of 0.2 mm. The profile taken to show the rotational transitions had an additional 8-pixel moving average applied.

4. Results and discussion
   4.1. TGS characterization
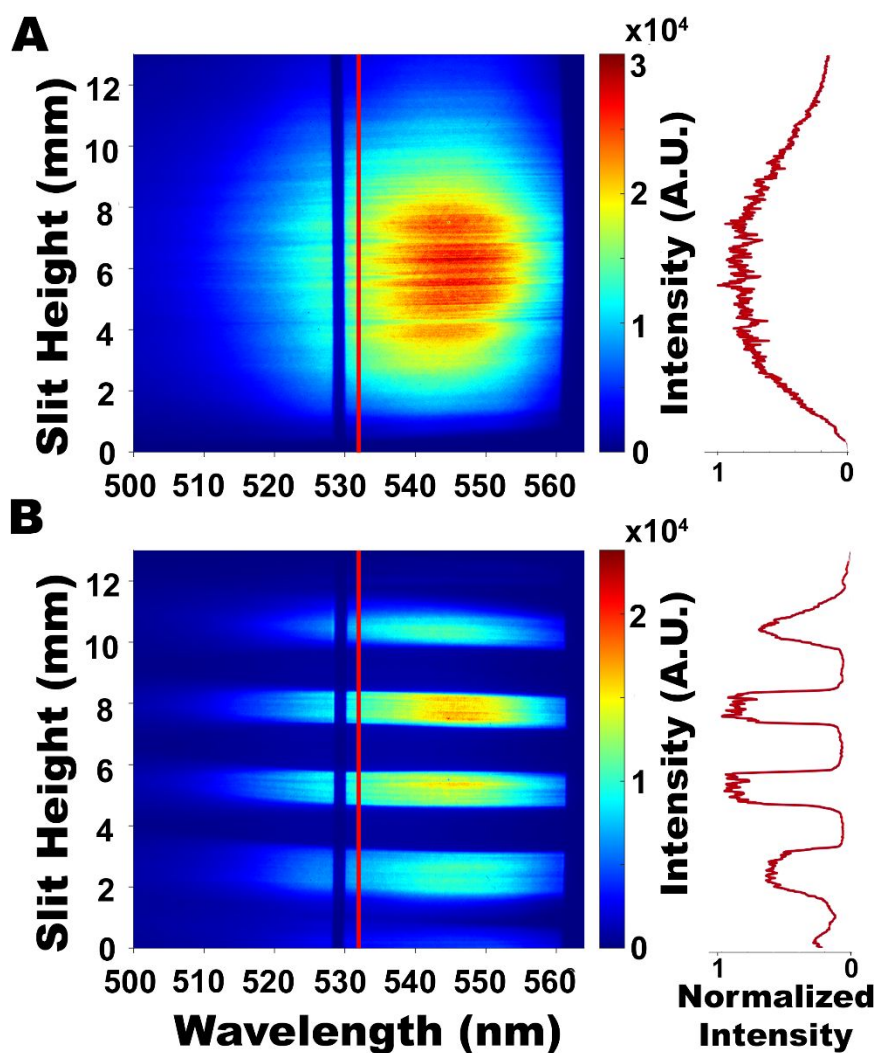
Figure 2. (A, left) Flatfield image and (B, left) spatial resolution image taken at 1x1 iCCD binning. The dark vertical section centered at ~529 nm shows the shifted location of the 0.33 mm wide mask and the red lines at 532 nm show the corresponding profile locations (A and B, right). The mask was moved to gauge the spatial resolution and intensity variations at the center of our wavelength window of interest. Spherical aberrations, field curvature, and heterogeneous pixel responses are evident.

It is well-known that imaging systems can be significantly affected by many different aberrations resulting from the inherent optical components, or alignment including astigmatism, spherical, comatic, keystone, chromatic, etc. [63, 64]. Furthermore, iCCD cameras are known to suffer from hot/cold pixels and pixel-to-pixel sensitivity variations [65]. Therefore, it is imperative to perform a flatfield correction to normalize raw images to the flatfield for minimization of the spectrograph's heterogeneous intensity distribution. The flatfield response of the TGS is shown in Fig. 2A. Spherical aberrations and field curvature are apparent, characterized by the decreasing intensity from the center

of the image outward towards the edges, more clearly displayed by the vertical intensity profile on the right (see Fig. 2A). Variations in the spectral dimension are also significantly affected by the inherent spectral shape of the LED source.

The spatial resolution is an important parameter when designing an imaging system for Thomson scattering plasma diagnostics. Consideration must be given to the size and separation distances for the objects of interest. Chemical analysis plasmas can range from 1-10's of mm (e.g. GDs and ICPs) down to sub-mm diameters (e.g. ambient ionization plasma jets for MS). Therefore, to have a sufficient number of radial points a resolution of ≤ 0.5 mm is desirable for larger plasmas and ≤ 0.05 mm for the smaller ones. This TGS was designed to have a theoretical spatial resolution (R_{spat}) of ~50 µm, with no binning in the spatial dimension, approximated by the following equation [66-68]

$$R_{spat} \approx h_{pix} * Pix_{min} * Pix_{bin} * Er_I \tag{1}$$

where h_{pix} is the height of 1 pixel on the iCCD camera (13 µm), Pix_{min} is the minimum number of pixels that need to be covered to be considered resolved (2.5), Pix_{bin} is the number of binned pixels (1), and Er_I is the estimated error due to the intensifier and gain of the camera (1.5). The line-spread function (LSF) was obtained by taking the first derivative (see SF3) of the intensity profile across the spatial dimension (see Fig. 2, right). The full width at half maximum (FWHM) of the peaks in the LSF plot at the line-mask edge locations provide the distance required for the edge response to rise from the minimum to the maximum values, which is characteristic of the spatial resolution [69]. At 532 nm, the spatial resolution ranges from 0.18 – 0.20 mm in the slit height region between 4 mm and 10 mm, while in the region of < 4 mm and > 10 mm it degrades to 0.56– 1.1 mm due to the evident increasing aberrations further from the center (see Fig. 2A and SF3).
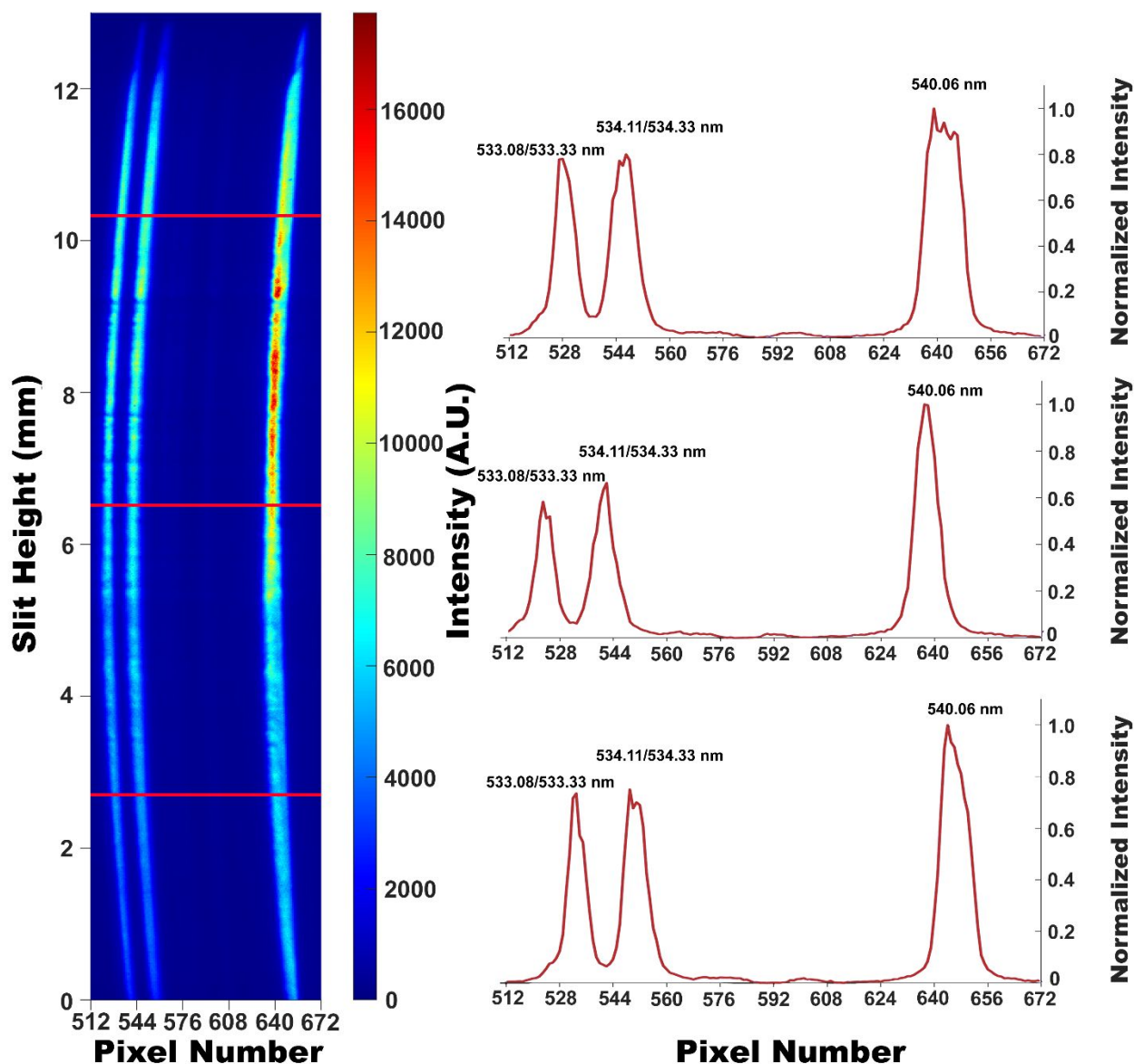
Figure 3. Spectral image (left), 1x1 binning, of a Ne pen-ray lamp source. Differences in smile and FWHM across the image are apparent. The red lines correspond to the location of the selected spectra (right) showing the peak shape more clearly.

The spectral resolution is another vital parameter that needs to be carefully considered for an adequate number of wavelength channels to be resolved from one another. Chemical analysis plasmas generally see Thomson scattering wavelength shifts that are ≤ 5 nm from the central wavelength, typically in the range of ~0.5 - 3 nm, due to the relatively low T_e. The slit widths (w_{slit}) are the limiting aperture in terms of the spectral bandpass for our system and were chosen to be 52 μm, thus giving a theoretical spectral resolution (R_{spec}) of ~0.6 nm as approximated by the following equation [66, 68]

$$R_{spec} \approx w_{slit} * Pix_{min} * Pix_{bin} * \frac{\delta\lambda}{\delta L} \qquad (2)$$

where $Pix_{min} = 2.5$ and $\delta\lambda/\delta L$ is the reciprocal linear dispersion (4.81 nm/mm). The w_{slit} chosen was a trade-off between light throughput, which is directly proportional to the area of the slit, and the spectral resolution. The smile can be clearly seen in Fig. 3 by the non-linear vertical bands and is further seen in the offset profiles to the right. Shift values, with respect to the center of the slit height (6.5 mm), due to the smile are 9 pixels at 10.5 mm, and 5 pixels at 2.7 mm. The peaks at 533.08/533.33 nm and 534.11/534.33 nm are double bands that cannot be resolved in our system. The 540.06 nm line FWHM values as a function of slit height are 0.75 nm at 10.4 mm, 0.44 nm at 6.5 mm, and 0.63 nm at 2.6 mm. The Ne spectrum was then subsequently used to perform a row-by-row spectral calibration to correct for the smile.
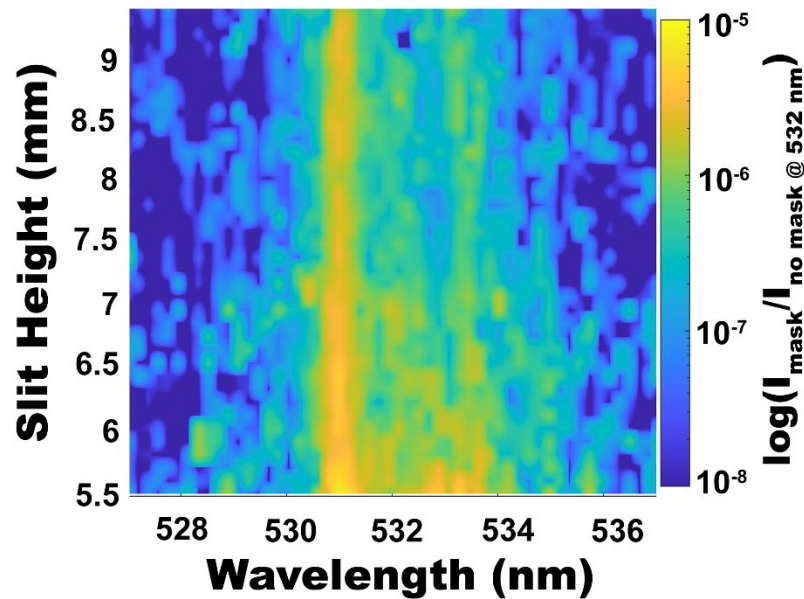
Figure 4. Contrast image (cropped to our region of interest), showing the efficiency of the TGS narrowband notch filter using a 0.33 mm mask at 532 nm. The contrast achieved is $\leq 10^{-6}$ at ± 0.5 nm wavelength shifts. Refer to experimental details (Section 3) for pixel/interpolation step size and to Figs. 2B and 3 for the spatial/spectral resolution, respectively.

The contrast provided by the notch filter is an extremely important value to take into account for Thomson scattering measurements. It is desirable to achieve a 10^{-6} contrast at wavelength shifts as close as ± 0.5 nm for low-density plasmas used for chemical analysis. The mask width of 0.33 mm was chosen to provide this attenuation while being able to measure scattering as close as 532 ± 0.75 nm. The images were

cropped to provide a representative contrast for our regions-of-interest (ROI) both spatially (5.5 - 9.4 mm slit height) and spectrally (527 - 537 nm). The spectral ROI is determined by the plasmas inherent T_e and the corresponding width of the scattering signal, while the spatial ROI is limited by the area where the appropriate spatial resolution is achieved. The contrast as a function of spatial position is shown in Fig. 4 and is calculated at each slit height by dividing the intensity with the 0.33 mm mask in place at each wavelength channel, by the intensity at 532 nm with the mask removed. Specifically, the spectral area that the 0.33 mm mask covers (532 ± 0.75 nm) has contrast values ranging from $\sim 1 \times 10^{-7}$ in the center to $\sim 5 \times 10^{-6}$ at the edges. In the region of 0.75 - 1 nm wavelength shifts from 532 nm, the poorest contrast is $\sim 8 \times 10^{-6}$, which is observed at 531 nm and a slit height of 5.5 mm. The contrast improves at farther than 1 nm wavelength shifts and is generally $< 10^{-7}$ at more than 532 ± 2 nm. Therefore, the resulting contrast has a value of $\leq 10^{-6}$ at 532 ± 0.5 nm across the ROI for this TGS design. This level of contrast allows access to Thomson scattering at relatively low n_e values that are found in close proximity to highly reflective surfaces/walls. Furthermore, the stray light that is effectively distributed across the entire detector was characterized in a similar way to the contrast, except at much farther wavelength shifts (± 22-32 nm) from 532 nm. The average stray light rejection across all slit heights, at 532 ± 22-32 nm, is $\sim 1.8 \times 10^{-8}$ with a corresponding standard deviation of $\sim 3.1 \times 10^{-7}$.

An imaging characterization at the object was also performed. Using the collection optics described above (see Table 1) a magnification of 1:1 from the plasma/laser interaction region to the entrance slit (S1) of the TGS is achieved. The 135° collection angle must be taken into account for calculating the appropriate spatial values since ~1.4 mm along the laser axis corresponds to ~1 mm at the iCCD detector. Figure SF4 shows the flatfield image obtained that is used to correct all subsequent images taken at the laser/plasma interaction region for imperfections in the imaging system and the iCCD pixel-sensitivity variations.
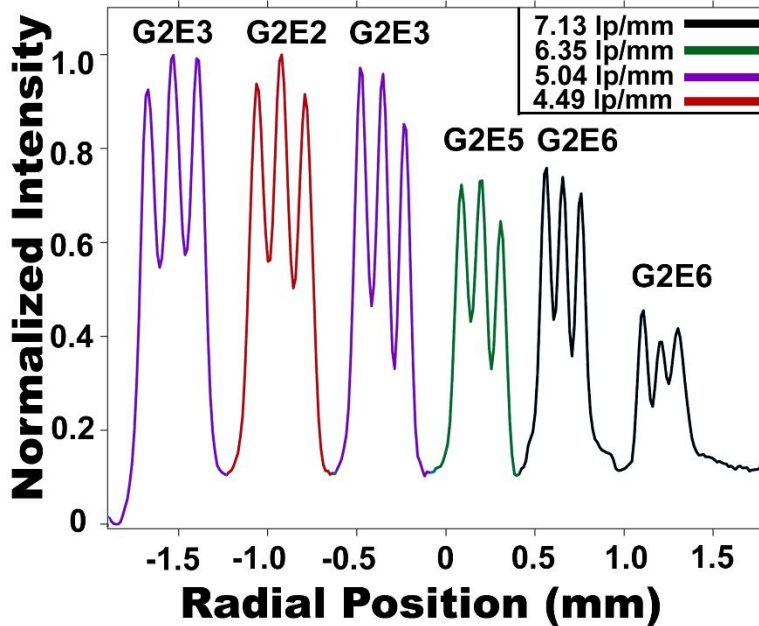
Figure 5. Spatial intensity profiles, at 1x1 binning measured using a 1951 USAF target oriented along the laser axis, at the GD chamber. The elements shown are the smallest elements that could be resolved at a peak-to-valley ratio of 2. The 0 mm radial position corresponds to the plasma axis.

Fig. 5 shows the spatial resolutions at a peak-to-valley ratio (P/V) of ~2, along the laser axis. The spatial resolution as a function of radial position has a range of 4.49 - 5.04 line pairs (lp)/mm from 0 to -2 mm and 6.35 - 7.13 lp/mm from 0 to 2 mm. Therefore, the minimum spatial resolution across the entire ROI, under the criteria stated, is $\leq$ 4.49 lp/mm (~110 μm/line).

4.2. Rayleigh scattering

Proof-of-principle Rayleigh scattering measurements of n_g and T_g were performed on a GD plasma with the newly characterized TGS system. A GD operated under typical conditions used for OES served as a model system given its low-density plasma characteristics, as well as some fundamental parameter measurements available in the literature for comparison. GDs used under typical OES conditions have been reported to have n_e as low as ~10^9 cm^{-3} and a T_e of ~0.05 eV for thermalized electrons [26, 37, 70]. Plasma heating effects are known to be worse at lower T_e and higher n_e values so caution must be taken to ensure perturbation is minimized through control of the laser fluence. Taking into account the worst-case scenario for GD operated under chemical analysis conditions, the T_e is ~0.05 eV and the n_e is ~10^{14} cm^{-3}, a laser fluence of ~$20*10^4$ J/m^2 results in a fractional plasma heating at ~0.1%, which is insignificant for T_e calculations [71].
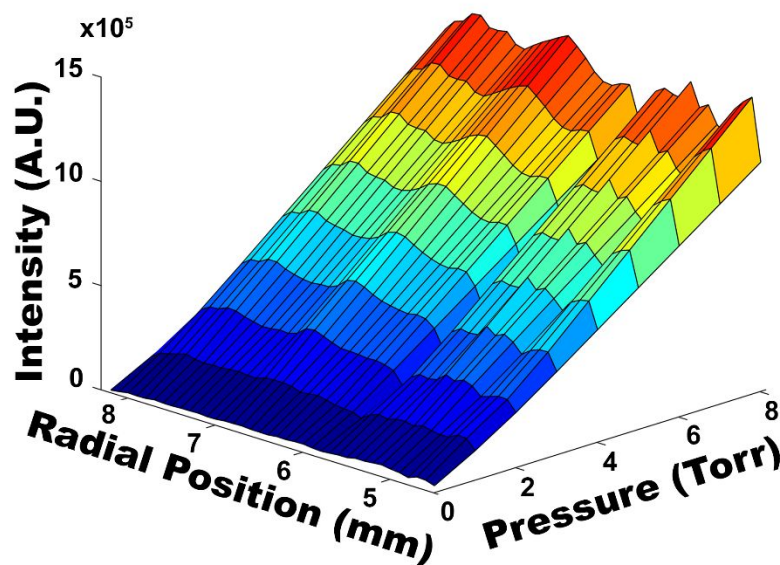
Figure 6. Rayleigh scattering pressure calibration as a function of radial position, with the plasma off, showing the linear relationship between scattering intensity and pressure. The stray light has an average value of 7.9 mTorr with a standard deviation of 6.7 mTorr across the ROI. Radial position of 0 is the axis of plasma.

Rayleigh scattering was first utilized to calibrate the scattered signal at known pressures (0-8 Torr) and temperature (ambient), with the plasma off, as a function of spatial position (see Fig. 6). The physical mask was removed to allow the 532 nm band to pass through the TGS to the iCCD. This reference measurement was subsequently used for the absolute T_g to be measured with the plasma on, at a known pressure. Furthermore, the Rayleigh signal was used to absolutely calibrate the scattering response for the calculation of n_e via Thomson scattering, shown below. The radial positions monitored were offset 4.5 mm from the center of the GD chamber in an effort to probe the edge of the negative glow region, so significant changes in T_g could be observed. The stray light value at the y-intercept, equal to the scattering signal at 0 Torr, had an average value of 7.9 mTorr, (standard deviation = 6.7 mTorr, minimum = 0.71 Torr, maximum = 21 mTorr) across the entire ROI. This is 2 orders-of-magnitude lower in comparison to the double monochromator used to measure a DC GD by Gamez et al. in 2003, which had a value of ~350 mTorr [37].
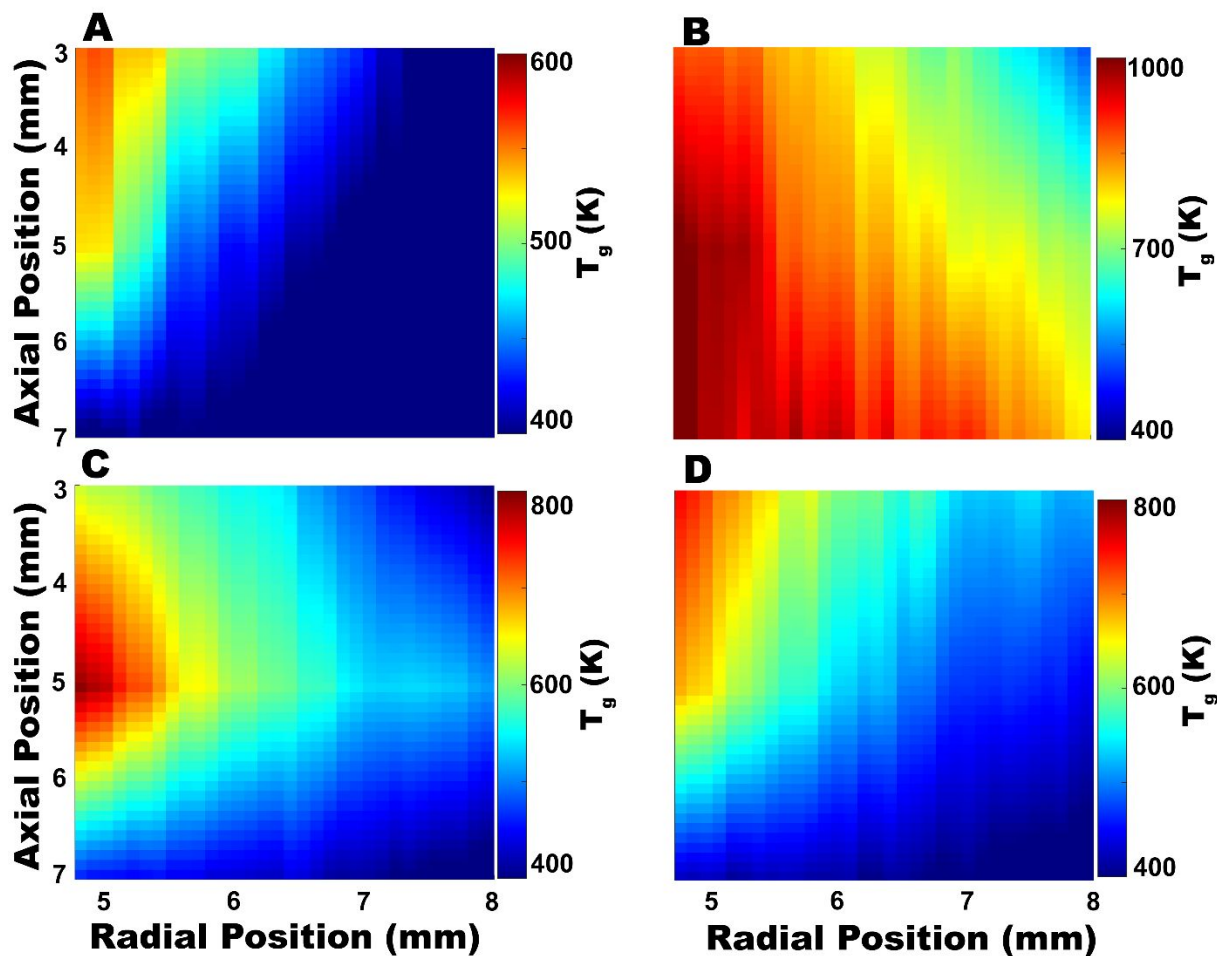
Figure 7. T_g maps at the edge of the negative glow region: 3.10 Torr, (A) 450 V, 10 mA, 0.047 W/mm², (B) 800 V, 30 mA, 0.25 W/mm²; and 7.20 Torr, (C) 450 V, 10 mA, 0.047 W/mm² (B) 800 V, 30 mA, 0.25 W/mm². Axial position 0 is defined as the cathode surface and radial position of 0 is the axis of plasma. Note that each image has a colormap scale normalized to its own maximum T_g.

Once the calibration was performed with the plasma off, the n_g was successfully measured with the plasma on, at three different axial positions (3, 5, 7 mm) to create a 2D spatial map shown in Fig SF5. The n_g is directly proportional to the intensity of the Rayleigh scattering signal as demonstrated by the pressure calibration in Fig. 6. The calibration was then used to calculate 2D spatial maps of the absolute T_g via the ideal gas law (see Fig. 7A-D). At 3.10 Torr (10 mA, 0.047 W/mm²) the maximum T_g of ~550 K is observed closest to the cathode surface, at 3 mm axially and 5 mm radially (see Fig. 7A). The T_g is then observed to decrease as a function of increasing radial/axial positions until reaching a minimum of ~340 K at the edge of the map. The higher pressure of 7.20 Torr (10 mA, 0.047 W/mm²) shows a higher maximum T_g of ~800 K at 5 mm radially/axially,

dropping to ~600 K at 6.5 mm (see Fig 7C). Interestingly, the maximum is observed further from the cathode surface. However, further systematic studies are required to confirm this feature and elucidate the possible mechanisms. At 3.10 Torr (30 mA, 0.25W/mm^2) the maximum T_g of ~1000 K is once again found at 5 mm axially/radially, while it drops to ~800 K at 6.5 mm (see Fig. 7B). The higher power case at 3.10 torr (see Fig. 7B) shows an enlargement of the area dominated by higher temperatures, in comparison to the lower power case, which is expected due to higher current/voltage being applied. At 7.20 Torr (30 mA, 0.25 W/mm^2) a similar T_g trend as 7.20 Torr 10 mA case is observed, with a slightly lower maximum of ~750 K closest to the cathode, dropping to ~600 K at 6.5 mm spatially/radially. Furthermore, a contraction of the higher temperature region from 3.10 torr (see Fig 7B) to 7.20 torr (see Fig 8D) at the high-power conditions is seen, due to a shorter mean-free path in the plasma. Previous Rayleigh scattering studies on a DC GD (3 Torr, 10 mA, 0.038 W/mm^2) reported a T_g of ~600 K (4 mm from the cathode at the plasma axis) dropping to ~350 K (8 mm from the cathode), which is comparable to the results here (see Fig 7A), considering the differences in operating conditions (ROI: negative glow edge vs axis; cathode material: SS vs. Cu; and interelectrode distance: 35 mm vs 50 mm)[41]. Furthermore, simulations performed by Bogaerts et al. in 2004 under the same conditions give a T_g of ~600 K (3 mm axially) dropping to ~475 K (8 mm axially), which also shows good agreement with our study, within experimental differences [72]. In particular, the model calculated T_g values are known to depend strongly on the assumed cathode temperature (550 K), which was not monitored for our current study [73].

4.3. Thomson scattering
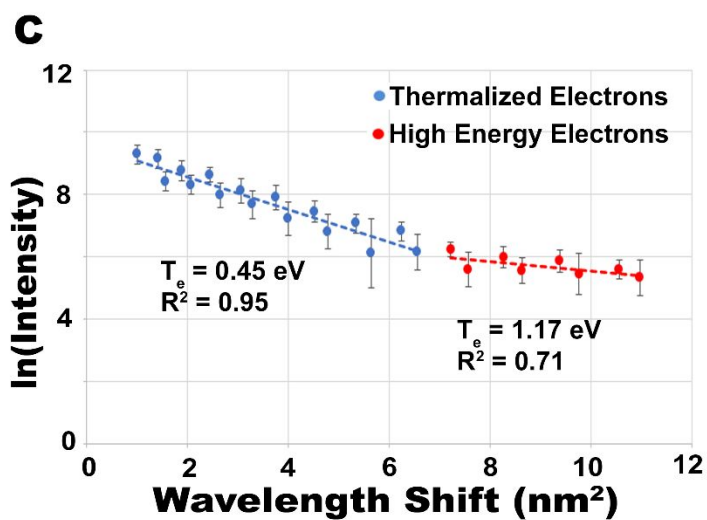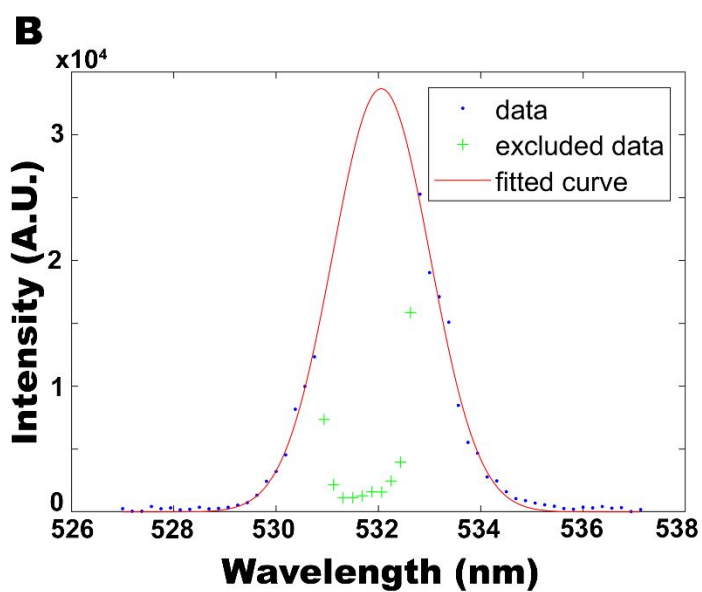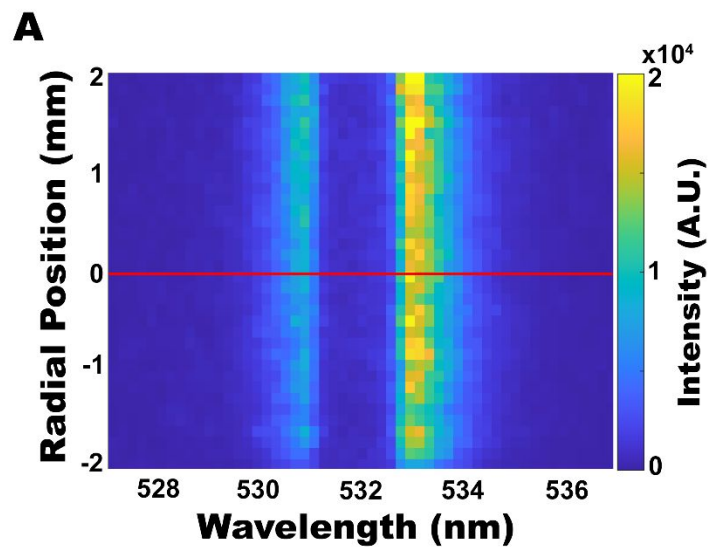
Figure 8. (A) Thomson scattering spectral image for a 2 ms-pulsed RF plasma at 7.05 Torr and a self-bias of 500 V, taken 2.5 mm from the cathode, at 3x8 iCCD binning. The low-intensity band seen at 532 nm shows the location of the physical mask. Red line shows the radial location of the spectrum used for (B) the Gaussian fit to extract the n_e and (C) the linearized Thomson spectrum used to extract T_e. The error bars represent 1 standard deviation between the 5 replicate data sets.

The ability to obtain Thomson scattering spectra from a ms-pulsed RF GD with the newly developed TGS was also tested. Fig. 8A shows the resulting Thomson scattering image after applying the corrections and filtering described previously in the methods section. Moreover, this image was taken at the axial position of the plasma, at 2.5 mm from the cathode to give a relatively high n_e and thus scattering signal for subsequent LOD calculations. Thomson theory states that the Doppler broadened scattering should be symmetric which is seen by the width of the spectrum but not the peak intensities. This asymmetry of the intensity peaks is due to the off-center orientation of the mask seen clearly by the profile in Fig. 8B. The off-center orientation of the mask was necessary to achieve the $< 10^{-6}$ contrast (see Fig. 4) due to the smile of the image when it is spatially filtered by the straight physical mask. If the EEDF is Maxwellian and the scattering is incoherent, a spectrum with a Gaussian distribution will be observed and the linearized Thomson profile will show a straight line. An example of a Gaussian fitted profile for extracting the absolutely calibrated n_e based on the unique Raman scheme discussed in the methods section is also seen in Fig. 8B with the area covered by the mask excluded from the fit. Furthermore, it is evident from the linearized spectrum (see Fig 8C) that the data is better described by a fit of two independent lines. The criteria used to separate the data into two groups was when the slope of the line changed by $> 5\%$ upon the addition of a new data point. This behavior is indicative of a bi-Maxwellian distribution where the two linear fits correspond to a lower energy (thermalized) group and a higher energy group. Previous TS studies on DC GD performed under similar conditions also showed this type of trend [37, 42].

The error bars seen in Fig. 8C are calculated from 1 standard deviation between the 5 replicates which has a maximum of 1.1, minimum of 0.24, and an average of 0.42 for the thermalized electrons. The high energy electrons have a maximum of 0.67, minimum of 0.23, and an average of 0.43. The RSD in the slope of the linear regressions seen in Fig. 8C were found to be ~6% for the thermalized electrons and ~38% for the high energy electrons after plotting/fitting all the replicate data points simultaneously. These two values are used for the error in the T_e calculations since those values are directly inversely related to the slope of the fit. The error in the 2D maps for the thermalized group's T_e shown below was also evaluated in the same way. The error in the

T_e is expected to be worse at lower n_e values due to the corresponding lower scattering intensity and was measured to be ~18% and ~13% at 10^{11} cm^{-3} and 10^{13} cm^{-3} respectively. In contrast, the n_e measurement accuracy relies heavily on the goodness-of-fit for the Gaussian curve. The R^2 values (adjusted for the degrees-of-freedom) of the fit vary between ~0.85 - 0.99 for all the fits used in calculating the 2D n_e maps shown below. The χ^2 value obtained from plotting all the replicate data points simultaneously was then related to the corresponding standard deviation of the Gaussian fit and subsequently divided by the area of the fit to calculate RSD. Due to the direct relationship between the n_e and the area of the fit, this is representative of the n_e error. The RSD values were seen to vary between ~8 and ~14% for n_e values of 10^{13} cm^{-3} and 10^{11} cm^{-3}, respectively.

It is also noteworthy to mention that due to lower stray light values and higher contrast close to the laser wavelength, Thomson measurements were able to be taken at 2.5 mm from the cathode which is closer than the 4 mm obtained by Gamez et al. previously with the double monochromator arrangement [41]. The limit-of-detection (LOD) in terms of n_e was then estimated using a similar calculation to that by M. J. van de Sande [32, 36] on the scattering signal seen in Fig. 8B. The standard deviation of the background signal between the 5 replicate measurements is ~40 counts at the 1/e height of the spectrum. The intensity value corresponding to this 1/e height is ~12,500 counts and the S/N is thus ~300. The n_e of this plasma, calculated from the Gaussian fit in Fig. 8B is on the order of ~10^{13} cm^{-3}. Therefore, the LOD where the S/N ratio is 3 would be a factor of $(300/3)^2$ lower, which is ~10^9 cm^{-3}. Furthermore, this value depends on the T_e of plasma being measured, the binning applied and pixel size of iCCD, and the integration time. Therefore, the LOD will only be accurate for the conditions used here (10 min integration time, 8x binning spatially for 13μm pixel height, and ~1 eV T_e). Nonetheless, the LOD seen here is an order-of-magnitude lower than LODs published for the other Thomson instruments described previously under similar conditions [36, 59]. For comparison, using a TGS instrument, n_e detection limits were reported on the order of ~ 10^{10} cm^{-3} using 3x longer integration times (30 min), on a plasma with ~1 eV T_e [36].
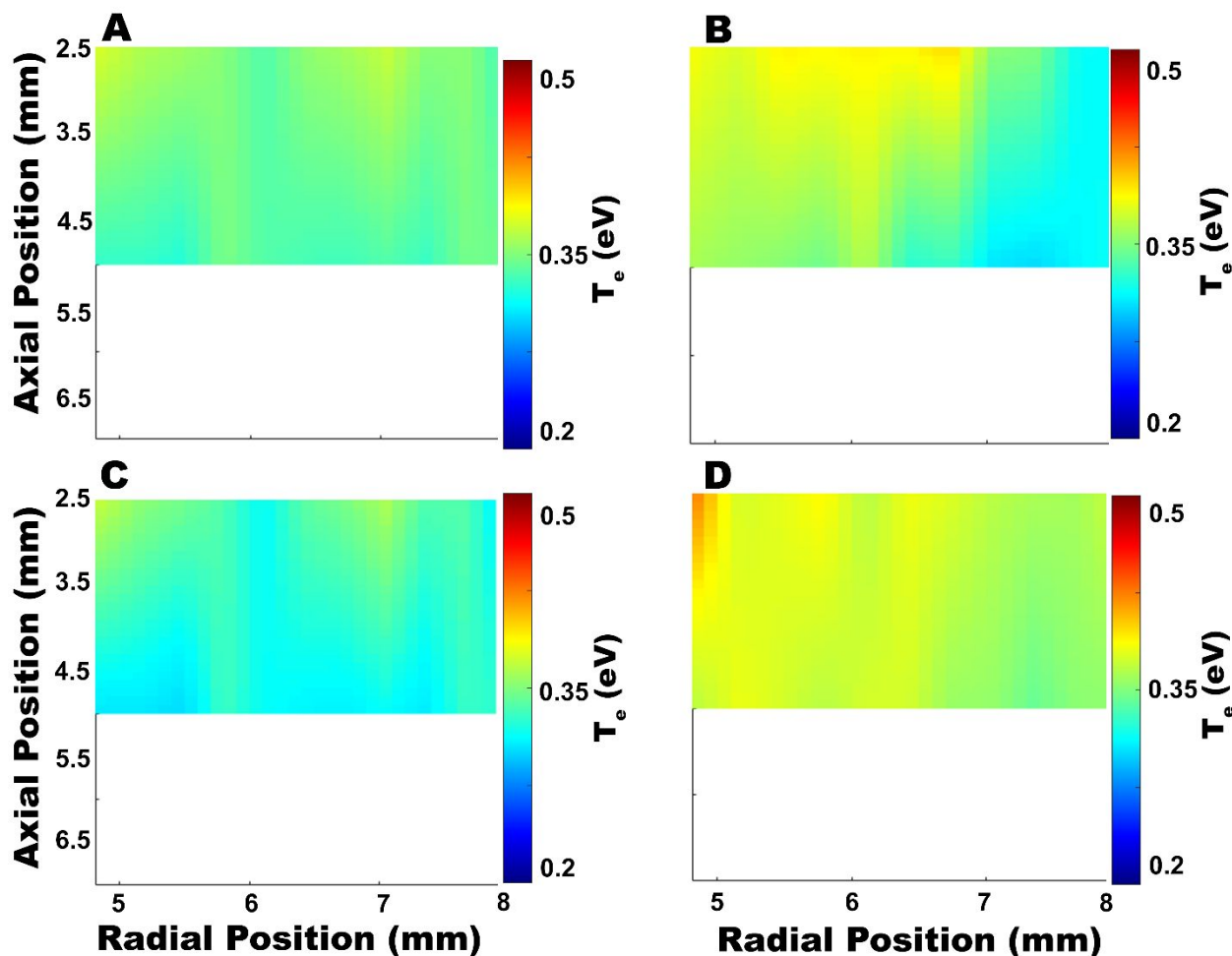
Figure 9. 2D T_e maps showing the energy distribution of free electrons at the edge of the negative glow region. Maps were taken at 4 different RF conditions, 3.10 Torr: (A) 450 W forward power, 115 W reflected power, 250 V_{dc} self-bias (B) 800 W forward power, 250 W reflected power, 500 V_{dc} self-bias and 7.05 Torr: (C) 450 W forward power, 115 W reflected power, 250 V_{dc} self-bias (D) 800 W forward power, 250 W reflected power, 500 V_{dc} self-bias. Axial position 0 is defined as the cathode surface and radial position of 0 is the axis of plasma.
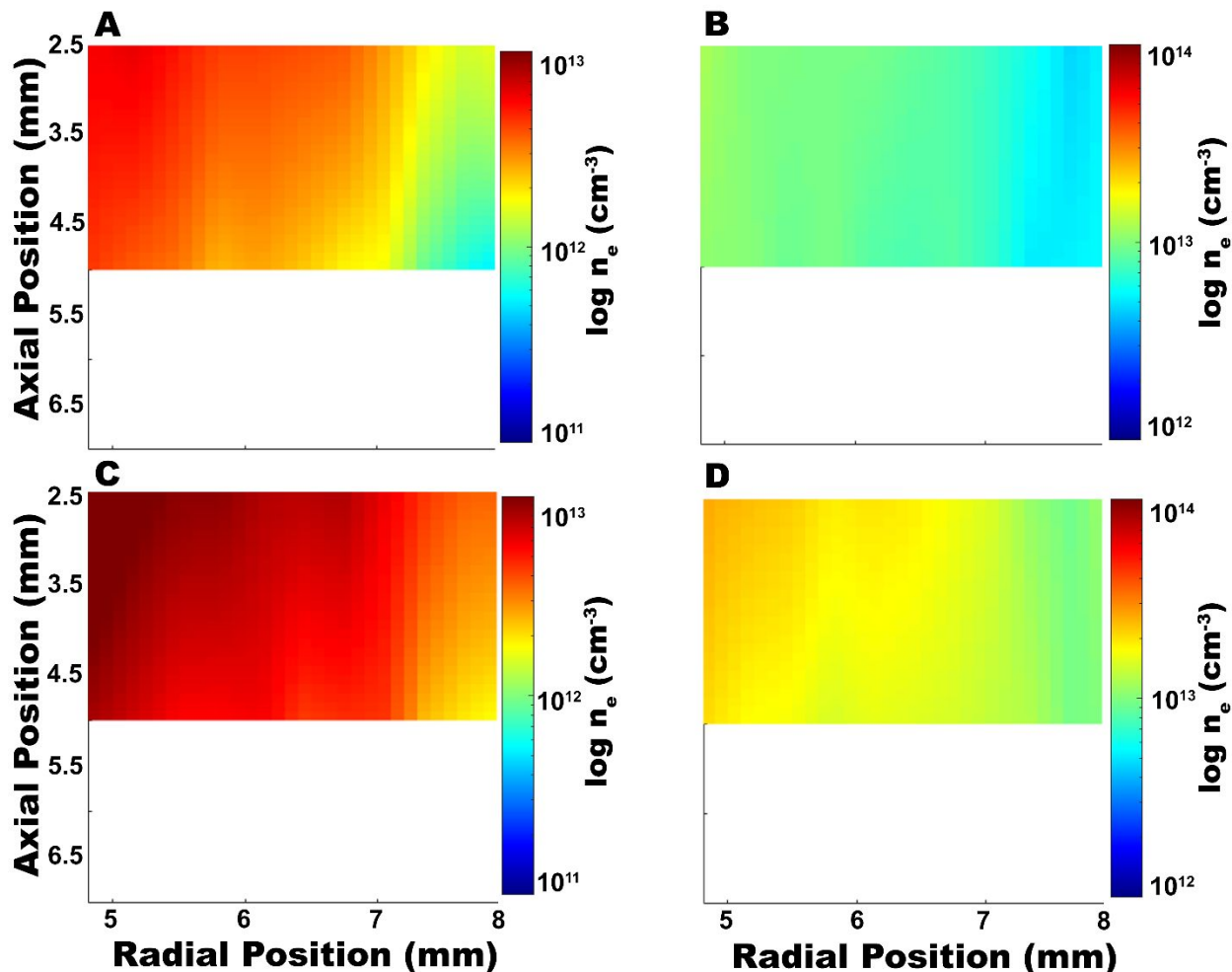
Figure 10. 2D n_e maps showing the number density distribution of free electrons at the edge of the negative glow region. Maps were taken at 4 different RF conditions, 3.10 Torr: (A) 450 W forward power, 115 W reflected power, 250 V_{dc} self-bias (B) 800 W forward power, 250 W reflected power, 500 V_{dc} self-bias and 7.05 Torr: (C) 450 W forward power, 115 W reflected power, 250 V_{dc} self-bias (D) 800 W forward power, 250 W reflected power, 500 V_{dc} self-bias. Note that each image has a colormap normalized to its own maximum feature. Axial position 0 is defined as the cathode surface and radial position of 0 is the axis of plasma.

2D maps were then obtained by probing 2 different axial positions (2.5 and 5 mm) for T_e (thermalized energy group, see Fig 9A-D) and n_e (see Fig 10A-D) under selected ms-pulsed RF conditions, using both 250/500 V_{dc} self-biases at 3.10 and 7.05 Torr. The larger axial scale than measurements were taken was chosen to match the scales seen in

the T_g (see Fig 7A-D) and n_g maps (see SF5A-D) for ease of comparison. At 3.10 Torr and 250 V_{dc} self-bias the T_e changes that are not very drastic within the ROI, but the T_e can be seen to decrease from 2.5 mm to 5 mm, with overall values of ~0.33 eV (see Fig. 9A). At higher pressure (7.05 Torr, 250 V_{dc} self-bias), a similar distribution inside the ROI is displayed, but with greater overall T_e of ~0.35 eV (see Fig. 9C). The T_e maps taken at 500 V_{dc} self-bias show more discernible radial changes. At 3.10 Torr, 500 V_{dc} self-bias, the T_e is ~0.38 closest to the cathode with the values decreasing to ~0.30 eV at the farthest position (see Fig. 9B). At 7.05 Torr, 500 V_{dc} self-bias, the trend is similar with slightly higher values, with a maximum of 0.43 eV and a minimum of ~0.35 eV (see Fig 9D). The range of measured T_e here agrees with values found in the literature, taking into account differences in operating conditions (spatial locations observed, cathode composition, and plasma geometry, etc.). For example, the bi-Maxwellian T_e distribution measured previously at the axial position in the plasma (see Fig. 8C) agrees within reason to DC GD experiments performed by Gamez et al. in 2006 on a planar-cathode DC GD at 3 Torr, 520 V, 35 mA which obtained T_e of ~0.30 for thermalized electrons and ~0.90 eV for the higher energy electrons at 4 mm from the cathode surface and at the axial position of the discharge [41]. Moreover, previous TS measurements on a DC GD with a Cu cathode show T_e values of ~0.3 eV for measurements taken from 4-6 mm from the cathode at 3 Torr, 520 V, 35 mA conditions [42]. Fang and Marcus, performed Langmuir probe measurements on a planar-diode DC GD at 2 Torr, 10 mA, 600 V for a Ni cathode and obtained values of ~0.25 eV T_e at a distance of 5.4 mm from the cathode [70]. Furthermore, the trends with respect to current observed here were also seen in those previous studies [41, 70].

The spatial n_e distribution changes over the ROI are more significant in contrast to the T_e. At 3.10 Torr, 250 V_{dc} self-bias, the n_e values range from ~4 × 10^{12} cm^{-3} closest to the cathode to ~6 × 10^{11} cm^{-3} farthest away (see Fig. 10A). When the power is increased to 500 V_{dc} self-bias, the n_e is observed to increase, reaching a maximum of ~2 × 10^{13} cm^{-3} closest to the cathode and a minimum of ~5 × 10^{12} cm^{-3} (see Fig 10B). Similar trends are observed at the higher pressure, 7.05 Torr, with overall higher n_e in comparison to the corresponding 3.10 Torr maps. At 7.05 Torr, 250 V_{dc} the n_e has a maximum value of ~1 × 10^{13} cm^{-3} closest to the cathode and decreases to ~3 × 10^{12} cm^{-3} farthest away. As the power is increased to 500 V_{dc} self-bias at 7.05 Torr, the n_e is observed to increase further with a maximum of 3 × 10^{13} cm^{-3} closest to the cathode and decreases to 1 × 10^{13} cm^{-3} farthest away. In 1999, Monte Carlo modeling by Bogaerts et al. gave the same order-of-magnitude n_e of ~10^{11}-10^{13} cm^{-3} for thermalized electrons from a Grimm-type RF GD at 5.8 Torr, ~600 V_{dc} self-bias, taken between 1-6 mm from the cathode, as is measured during this study [74]. Furthermore, Gamez et al. measured values between ~1-5 × 10^{12} cm^{-3} for thermalized electrons (~0.3 Torr) via Thomson scattering on a planar-cathode DC GD taken at the axial position of the discharge, from 4-8 mm from the cathode at 3 Torr,

520 V, 35 mA [41]. These values agree well with the measured n_e in this study, considering the experimental differences previously described.

4.4. Raman scattering
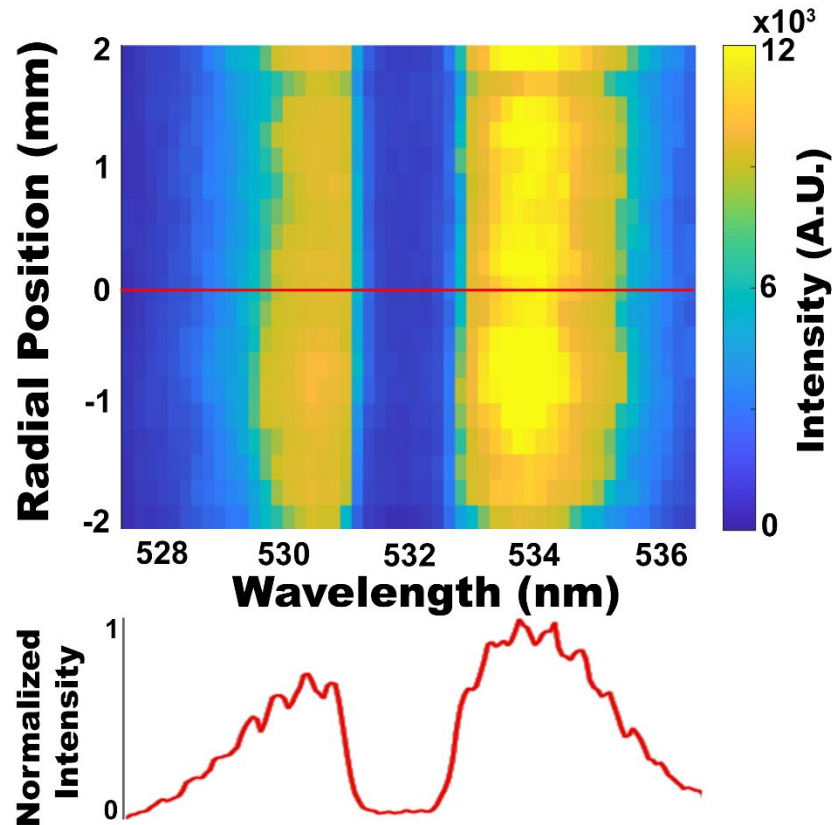
Figure 11. (top) N_2 rotational Raman scattering spectral image taken at atmospheric pressure, with the plasma off, at 3x8 binning. (bottom)The spectrum taken at the location of the red line under 1x1 binning shows distinct rotational transitions of N_2 after performing an 8-pixel moving average in the spatial dimension. Radial position of 0 is the axis of plasma.

As mentioned above, Raman scattering measurements were taken to perform day-to-day calibrations. Figure 11 is an example of a rotational Raman scattering spectral image showing the stokes and anti-stokes transitions of N_2 at atmospheric pressure. These demonstrated Raman scattering capabilities of the TGS instrument show the possibility to determine T_{rot} values. This will become especially useful in future studies of plasmas where N_2 is inherently present, such as atmospheric pressure plasma jets exposed to air for ambient mass spectrometry applications or GDs with nitride samples.

1
2
3
4
5
6
7
8
9
10
11
12
13
14
15
16
17
18
19
20
21
22
23
24
25
26
27
28
29
30
31
32
33
34
35
36
37
38
39
40
41
42
43
44
45
46
47
48
49
50
51
52
53
54
55
56
57
58
59
60

5. Conclusions and future work

A newly constructed TGS for improved chemical analysis plasma diagnostics has been designed, characterized, and the functionality verified through proof-of-principle measurements on continuous DC GD and ms-pulsed RF GD. This TGS features a high contrast of 10^{-6} at $\pm\ 0.5$ nm wavelength shifts from 532 nm with a high collection efficiency of F/2, which give access to relatively low n_e values close to highly reflective surfaces/walls that generate large amounts of stray light. This was experimentally verified by probing a RF GD via Thomson scattering at closer distances from the cathode surface compared to previous studies with a double monochromator instrument [41]. Rayleigh scattering measurements were successfully implemented to measure T_g and n_g, while allowing absolute calibration of the system for subsequent n_e measurements via Thomson scattering. Thomson scattering was successfully performed for the measurement of absolute n_e and T_e. Comparisons with previous studies verified the analytical performance of this newly designed instrument. The n_e LOD via Thomson scattering with was calculated to be $\sim 10^9$ cm^{-3} at 10 min integration time, 8x binning spatially for 13 µm pixel height, and ~ 1 eV T_e, which is 1 order-of-magnitude lower than previously reported under similar conditions [36, 59]. The measurement time reported here is more than an order-of-magnitude faster compared to literature values with double monochromator arrangements [41] and 3 times faster than TGS instruments [36] on similar plasmas, with reported higher LODs. Moreover, the current TGS design has a large spectral window (~ 64 nm total) which provides the ability to study chemical analysis plasmas with relatively high n_e and T_e (≥ 1 eV), such as laser-induced plasmas (LIPs), via laser-scattering techniques [35, 51, 75-80]. Due to the relatively small size of LIPs (commonly ≤ 1 mm), changes in the fundamental parameters can occur on spatial scales well within the laser beam diameter. This occurs when the LIP diameter $\leq$ laser beam diameter and results in TS spectra containing only line-of-sight integrated information. Furthermore, a limitation in the size of the focused beam arises due to plasma perturbations based on heating effects by using too high of a laser fluence (described in Section 4.2). In these cases, mathematical inversions such as the Radon/Abel transform [81, 82] would be necessary to obtain radially resolved fundamental information within the width of the laser beam, and Abel transform could be easily implemented on our instrument. Future studies include systematic spatiotemporal characterization of RF GD under OES elemental mapping conditions to characterize effects of higher pressure and pulsed-power mode operating conditions. Further characterization will then be performed on atmospheric pressure plasma jets used for ambient mass spectrometry and OES, such as dielectric barrier discharge (DBD) [83, 84] and low-temperature plasma (LTP) [1]. In this case, tighter focusing of the incident laser beam will allow measurements closer to surfaces/walls.

Acknowledgments

References

1. X. Gong, S. Shi and G. Gamez, *Journal of the American Society for Mass Spectrometry*, 2017, **28**, 678-687.
2. G. Gamez, S. J. Ray, F. J. Andrade, M. R. Webb and G. M. Hieftje, *Analytical Chemistry*, 2007, **79**, 1317-1326.
3. M. Bonta, J. J. Gonzalez, C. Derrick Quarles, R. E. Russo, B. Hegedus and A. Limbeck, *Journal of Analytical Atomic Spectrometry*, 2016, **31**, 252-258.
4. M. E. Monge, G. A. Harris, P. Dwivedi and F. M. Fernandez, *Chemical Reviews*, 2013, **113**, 2269-2308.
5. M. Schild, A. Gundlach-Graham, A. Menon, J. Jevtic, V. Pikelja, M. Tanner, B. Hattendorf and D. Günther, *Analytical Chemistry*, 2018, **90**, 13443-13450.
6. A. Bogaerts and R. Gijbels, *Spectrochimica Acta Part B: Atomic Spectroscopy*, 1998, **53**, 1-42.
7. M. Wilke, G. Teichert, R. Gemma, A. Pundt, R. Kirchheim, H. Romanus and P. Schaaf, *Thin Solid Films*, 2011, **520**, 1660-1667.
8. K. R. Marcus and J. A. C. Broekaert, *Glow Discharge Plasmas in Analytical Spectroscopy*, John Wiley & Sons, New York, 2003.
9. W. W. Harrison, *Journal of Analytical Atomic Spectrometry*, 1998, **13**, 1051-1056.
10. P. Belenguer, M. Ganciu, P. Guillot and T. Nelis, *Spectrochimica Acta Part B-Atomic Spectroscopy*, 2009, **64**, 623-641.
11. G. Gamez and K. Finch, *Spectrochimica Acta Part B: Atomic Spectroscopy*, 2018, **148**, 129-136.
12. G. Gamez, M. Voronov, S. Ray, V. Hoffmann, G. Hieftje and J. Michler, *Spectrochimica Acta Part B-Atomic Spectroscopy*, 2012, **70**, 1-9.
13. B. Busser, S. Moncayo, J. L. Coll, L. Sancey and V. Motto-Ros, *Coord. Chem. Rev.*, 2018, **358**, 70-79.
14. R. C. Wiens, S. Maurice, B. Barraclough, M. Saccoccio, W. C. Barkley, J. F. Bell, S. Bender, J. Bernardin, D. Blaney, J. Blank, M. Bouyé, N. Bridges, N. Bultman, P. Caïs, R. C. Clanton, B. Clark, S. Clegg, A. Cousin, D. Cremers, A. Cros, L. DeFlores, D. Delapp, R. Dingler, C. D'Uston, M. Darby Dyar, T. Elliott, D. Enemark, C. Fabre, M. Flores, O. Forni, O. Gasnault, T. Hale, C. Hays, K. Herkenhoff, E. Kan, L. Kirkland, D. Kouach, D. Landis, Y. Langevin, N. Lanza, F. LaRocca, J. Lasue, J.

Latino, D. Limonadi, C. Lindensmith, C. Little, N. Mangold, G. Manhes, P. Mauchien, C. McKay, E. Miller, J. Mooney, R. V. Morris, L. Morrison, T. Nelson, H. Newsom, A. Ollila, M. Ott, L. Pares, R. Perez, F. Poitrasson, C. Provost, J. W. Reiter, T. Roberts, F. Romero, V. Sautter, S. Salazar, J. J. Simmonds, R. Stiglich, S. Storms, N. Striebig, J.-J. Thocaven, T. Trujillo, M. Ulibarri, D. Vaniman, N. Warner, R. Waterbury, R. Whitaker, J. Witt and B. Wong-Swanson, *Space Science Reviews*, 2012, **170**, 167-227.

15. S. Grosse-Kreul, S. Hubner, S. Schneider, D. Ellerweg, A. von Keudell, S. Matejcik and J. Benedikt, *Plasma Sources Science & Technology*, 2015, **24**.

16. H. R. Griem, *Principles of Plasma Spectroscopy*, Cambridge University Press, Cambridge, 1997.

17. J. R. Chirinos, D. D. Oropeza, J. J. Gonzalez, H. Hou, M. Morey, V. Zorba and R. E. Russo, *Journal of Analytical Atomic Spectrometry*, 2014, **29**, 1292-1298.

18. J. A. M. van der Mullen and J. M. de Regt, *Fresenius' Journal of Analytical Chemistry*, 1996, **355**, 532-537.

19. M. Aghaei, H. Lindner and A. Bogaerts, *Journal of Analytical Atomic Spectrometry*, 2013, **28**, 1485-1492.

20. H. Ma, N. Taylor and P. B. Farnsworth, *Spectrochimica Acta Part B: Atomic Spectroscopy*, 2009, **64**, 384-391.

21. N. N. Sesi, D. S. Hanselman, P. Galley, J. Horner, M. Huang and G. M. Hieftje, *Spectrochimica Acta Part B: Atomic Spectroscopy*, 1997, **52**, 83-102.

22. M. Huang and G. M. Hieftje, *Spectrochimica Acta Part B: Atomic Spectroscopy*, 1985, **40**, 1387-1400.

23. G. Gamez, S. A. Lehn, M. Huang and G. M. Hieftje, *Spectrochimica Acta Part B: Atomic Spectroscopy*, 2007, **62**, 357-369.

24. G. Gamez, S. A. Lehn, M. Huang and G. M. Hieftje, *Spectrochimica Acta Part B: Atomic Spectroscopy*, 2007, **62**, 370-377.

25. J. M. de Regt, F. P. J. de Groote, J. A. M. van der Mullen and D. C. Schram, *Spectrochimica Acta Part B: Atomic Spectroscopy*, 1996, **51**, 1371-1383.

26. A. Bogaerts, *Journal of Analytical Atomic Spectrometry*, 2007, **22**, 13-40.

27. A. Bogaerts, A. Quentmeier, N. Jakubowski and R. Gijbels, *Spectrochimica Acta Part B: Atomic Spectroscopy*, 1995, **50**, 1337-1349.

28. M. Kuraica, N. Konjević, M. Platiša and D. Pantelić, *Spectrochimica Acta Part B: Atomic Spectroscopy*, 1992, **47**, 1173-1186.

29. I. H. Hutchinson, *Principles of Plasma Diagnostics*, Cambridge University Press, Cambridge, 2 edn., 2002.

30. T. K. Starn, N. N. Sesi, J. A. Horner and G. M. Hieftje, *Spectrochimica Acta Part B: Atomic Spectroscopy*, 1995, **50**, 1147-1158.

31. D. E. Evans and J. Katzenstein, *Reports on Progress in Physics*, 1969, **32**, 207-271.

32. M. J. v. d. Sande, 2002, DOI: 10.6100/IR554040.

33. A. Scheeline and M. J. Zoellner, *Appl. Spectrosc.*, 1984, **38**, 245-258.

34. A. B. Murphy, *Phys. Rev. E*, 2004, **69**, 1.

35. K. Dzierżęga, A. Mendys and B. Pokrzywka, *Spectrochimica Acta Part B: Atomic Spectroscopy*, 2014, **98**, 76-86.

36. M. J. v. d. Sande and J. J. A. M. v. d. Mullen, *Journal of Physics D: Applied Physics*, 2002, **35**, 1381-1391.

37. G. Gamez, M. Huang, S. A. Lehn and G. M. Hieftje, *Journal of Analytical Atomic Spectrometry*, 2003, **18**, 680-684.

38. H. J. Kunze, *Plasma diagnostics*, 1968.

39. C. Emile and N. Sander, *Plasma Physics and Controlled Fusion*, 2015, **57**, 014026.

40. H. Simon, S. Joao Santos, M. Joost van der and G. G. William, *Plasma Sources Science and Technology*, 2015, **24**, 054005.

41. G. Gamez, A. Bogaerts, F. Andrade and G. M. Hieftje, *Spectrochimica Acta Part B: Atomic Spectroscopy*, 2004, **59**, 435-447.

42. G. Gamez, A. Bogaerts and G. M. Hieftje, *Journal of Analytical Atomic Spectrometry*, 2006, **21**, 350-359.

43. K. Warner and G. M. Hieftje, *Spectrochimica Acta Part B: Atomic Spectroscopy*, 2002, **57**, 201-241.

44. M. Huang, K. Warner, S. Lehn and G. M. Hieftje, *Spectrochimica Acta Part B: Atomic Spectroscopy*, 2000, **55**, 1397-1410.

45. H. Kempkens and J. Uhlenbusch, *Plasma Sources Science and Technology*, 2000, **9**, 492-506.

46. A. F. H. van Gessel, E. A. D. Carbone, P. J. Bruggeman and J. J. A. M. van der Mullen, *Plasma Sources Science and Technology*, 2012, **21**, 015003.

47. M. Longenecker, L. Hüwel, L. Cadwell and D. Nassif, *Appl. Opt.*, 2003, **42**, 990-996.

48. A. W. DeSilva and G. C. Goldenbaum, in *Methods in Experimental Physics*, eds. H. R. Griem and R. H. Lovberg, Academic Press, 1971, vol. 9, pp. 61-113.

49. N. Chalyavi, P. S. Doidge, R. J. S. Morrison and G. B. Partridge, *Journal of Analytical Atomic Spectrometry*, 2017, **32**, 1988-2002.

50. M. Sneep and W. Ubachs, *Journal of Quantitative Spectroscopy and Radiative Transfer*, 2005, **92**, 293-310.

51. H. Zhang, Y. Wu, H. Sun, F. Yang, M. Rong and F. Jiang, *Spectrochimica Acta Part B: Atomic Spectroscopy*, 2019, **157**, 6-11.

52. McPherson, *https://mcphersoninc.com/pdf/Solution%20-%20Raman%20Commander.pdf*, *Accessed 5/29/20*.

53. Horiba, *https://www.horiba.com/uk/scientific/products/raman-spectroscopy/raman-spectrometers/triple-raman-spectrometers/details/triple-raman-spectrometers-140/*, *Accessed 5/29/20*.

54. X. Zhu, N. d. Vries, E. R. Kieft, J. J. A. M. v. d. Mullen and M. Haverlag, *Journal of Physics D: Applied Physics*, 2005, **38**, 1923-1935.

55. X. Zhu, M. Redwitz, E. R. Kieft, M. J. v. d. Sande and J. J. A. M. v. d. Mullen, *Journal of Physics D: Applied Physics*, 2004, **37**, 736-743.

56. M. J. v. d. Sande, R. H. M. Deckers, F. Lepkojus, W. Buscher and J. J. A. M. v. d. Mullen, *Plasma Sources Science and Technology*, 2002, **11**, 466-475.

57. T. D. Hettipathirana, *J Anal At Spectrom*, 2013, **28**, 1242-1246.

58. L. Yuan, J. n. Xie, Z. He, Y. Wang and J. Wang, *Opt. Express*, 2019, **27**, 17686-17700.

59. V. Benjamin, T. Sedina, M. Stéphane, M. Tiberiu and F. Jérôme, *Plasma Sources Science and Technology*, 2018, **27**, 055002.

60. P. Guo, J. Zhang, F. Yang and Y. Zhang, *The design and analysis of 2m telescope's K Mirror system*, SPIE, 2014.

61. C. A. Monnig, B. D. Gebhart and G. M. Hieftje, *Appl. Spectrosc.*, 1989, **43**, 577-579.

62. P. Bevington and D. K. Robinson, *Data Reduction and Error Analysis for the Physical Sciences*, McGraw-Hill, New York, 1969.

63. D. J. Schroeder, *Astronomical Optics 2nd Edition*, Academic Press, San Diego, 2000.

64. P. Mouroulis, R. O. Green and T. G. Chrien, *Appl. Opt.*, 2000, **39**, 2210-2220.

65. T. C. Williams and C. R. Shaddix, *Review of Scientific Instruments*, 2007, **78**, 123702.

66. J. M. Lerner, *Cytometry Part A*, 2006, **69A**, 712-734.

67. M. Saito, Y. Saito, K. Asamura and T. Mukai, *Review of Scientific Instruments*, 2007, **78**, 023302.

68. J. G. Robertson, *Publications of the Astronomical Society of Australia*, 2017, **34**, e035.

69. S. W. Smith, *The scientist and engineer's guide to digital signal processing*, California Technical Publishing, 1997.
70. D. Fang and R. K. Marcus, *Spectrochimica Acta Part B: Atomic Spectroscopy*, 1991, **46**, 983-1000.
71. E. A. D. Carbone, J. M. Palomares, S. Hübner, E. Iordanova and J. J. A. M. v. d. Mullen, *Journal of Instrumentation*, 2012, **7**, C01016.
72. A. Bogaerts, R. Gijbels, G. Gamez and G. M. Hieftje, *Spectrochimica Acta Part B: Atomic Spectroscopy*, 2004, **59**, 449-460.
73. A. Bogaerts, R. Gijbels and V. V. Serikov, *Journal of Applied Physics*, 2000, **87**, 8334-8344.
74. A. Bogaerts, R. Gijbels and W. Goedheer, *Spectrochimica Acta Part B: Atomic Spectroscopy*, 1999, **54**, 1335-1350.
75. N. Walsh, J. T. Costello and T. J. Kelly, *Applied Physics B*, 2017, **123**, 179.
76. G. A. Wubetu, T. J. Kelly, P. Hayden, H. Fiedorowicz, W. Skrzeczanowski and J. T. Costello, *Journal of Physics B: Atomic, Molecular and Optical Physics*, 2020, **53**, 065701.
77. M. Cvejić, M. R. Gavrilović, S. Jovićević and N. Konjević, *Spectrochimica Acta Part B: Atomic Spectroscopy*, 2013, **85**, 20-33.
78. A. Mendys, K. Dzierżęga, M. Grabiec, S. Pellerin, B. Pokrzywka, G. Travaillé and B. Bousquet, *Spectrochimica Acta Part B: Atomic Spectroscopy*, 2011, **66**, 691-697.
79. E. Nedanovska, G. Nersisyan, T. J. Morgan, L. Hüwel, T. Murakami, C. L. S. Lewis, D. Riley and W. G. Graham, *Journal of Applied Physics*, 2015, **117**, 013302.
80. K. Dzierżęga, W. Zawadzki, F. Sobczuk, M. L. Sankhe, S. Pellerin, M. Wartel, W. Olchawa, A. Bacławski and A. Bartecka, *Journal of Quantitative Spectroscopy and Radiative Transfer*, 2019, **237**, 106635.
81. D. N. Ghosh Roy, *Journal of Quantitative Spectroscopy and Radiative Transfer*, 1984, **31**, 15-21.
82. K. Dzierżęga, W. Zawadzki, B. Pokrzywka and S. Pellerin, *Physical Review E*, 2006, **74**, 026404.
83. S. Shi, X. Gong, Y. Mu, K. Finch and G. Gamez, *Journal of Analytical Atomic Spectrometry*, 2018, DOI: 10.1039/C8JA00235E.
84. S. Shi, K. Finch, Y. She and G. Gamez, *Journal of Analytical Atomic Spectrometry*, 2020, **35**, 117-125.